



Effects of ITO thin films on microstructural and photocatalytic properties of layered TiO₂/ITO films prepared via an extended deposition period

Kee-Rong Wu ^{a,*}, Chung-Hsuang Hung ^b, Meng-Hsiu Tsai ^c

^a Department of Marine Engineering, National Kaohsiung Marine University, Kaohsiung 811, Taiwan, ROC

^b Department of Safety, Health and Environmental Engineering, National Kaohsiung First University of Science and Technology, Kaohsiung, Taiwan, ROC

^c Metal Processing R&D Department, Metal Industries Research and Development Centre, Kaohsiung, Taiwan, ROC

ARTICLE INFO

Article history:

Received 20 March 2009

Received in revised form 12 August 2009

Accepted 19 August 2009

Available online 4 September 2009

Keywords:

Titanium dioxide

Tin indium oxide

Tin diffusion

Photocatalytic

Photoelectrochemical

ABSTRACT

This study elucidates how indium tin oxide (ITO) thin film affects the microstructural and photocatalytic properties of layered TiO₂/ITO films prepared by DC magnetron sputtering. Two ITO substrates, as-received ITO (aITO) and *in situ* sputtered ITO (sITO), are adopted herein. Photocatalytic measurements of methylene blue and dimethyl sulfoxide indicate that the layered TiO₂/sITO film has greater photocatalytic oxidation than the TiO₂/aITO catalyst. According to photoelectrochemical tests, the latter exhibits a completely opposite activity to that of the former. Secondary ion mass spectrometry elemental depth profiles reveal that tin atoms in the sITO film really permeate into the growing TiO₂ film and promote the formation of the crystalline Ti_{1-x}Sn_xO₂ layer. Additionally, cross-sectional transmission electron microscopy images and the selective area diffraction patterns show the difference between the diffusion of tin in the two catalysts. The photocatalytic oxidation capability is further enhanced in the layered TiO₂/sITO film because of an increase in the bandgap energy and a positive shift in the Fermi level energy of the Ti_{1-x}Sn_xO₂ layer. Conversely, tin diffusion is limited in the aITO substrate under controlled conditions, in such a manner that a Schottky barrier can form at the TiO₂/aITO interface. Therefore, photogenerated electrons can be efficiently transferred from the overlaid TiO₂ film to the aITO substrate, producing a remarkable photocurrent density under UV illumination. Microstructural measurements reveal that the growth of the reactive {0 0 1} facets and columnar porous structure are favored by the synergistic effect of ITO substrate and an extended period of deposition. Accordingly, the photocatalytic capabilities are further raised.

© 2009 Elsevier B.V. All rights reserved.

1. Introduction

Photocatalysis is a promising technique valuable for environmental and renewable energy applications. Among various semiconductor photocatalysts, titanium dioxide (TiO₂) is especially attractive for their non-toxic, clean and safe properties as well as their thermal stability and the abundance in the earth [1,2]. It has become one of the most suitable for widespread environmental applications, such as dye-sensitized photoelectrochemical (PEC) cells [3], gas sensors [4], self-cleaning surfaces, water splitting for hydrogen evolution, etc. [1,5]. Great efforts have been employed to facilitate charge transport and charge separation efficiency of TiO₂ thin film coupled with a large bandgap semiconductor, such as SnO₂ [6], amorphous WO₃ [7,8] and indium tin oxide (ITO) [9,10], or a high work function metal, e.g. Al,

Ti, Fe, Pd [11], Pt [12,13] and carbon nanotube [10,14–15] as heterostructured film electrodes. Layered TiO₂/ITO film is generally accepted to be an efficient heterostructure and provide a potential driving force for the separation of photogenerated charge carriers [9,16].

Recently, Dai et al. have reported that the layered TiO₂/ITO catalyst can benefit the photocatalytic (PC) reactions mainly inducing by the photogenerated holes rather than by the electrons [9]. This is because that ITO has a higher work function than TiO₂ and a depletion layer can form at the TiO₂/ITO interface, where the ITO thin film accepts electrons. The Schottky barrier height can enhance the photogenerated electron transfer from the TiO₂ film to the ITO substrate, leading a higher photocatalytic degradation rate over aqueous oleic acid solution. However, according to their X-ray photoelectron spectroscopy tests, no reaction occurs between TiO₂ and ITO substrate, which is prepared by dip coating route.

A TiO₂ film deposited on ITO substrate has a more crystalline structure than one deposited on other substrates, such as Si, glass, quartz or Al₂O₃ [16,17]. Anatase TiO₂ nanocrystalline films that were grown with a thickness of 5 μm on as-received ITO (aITO)

* Corresponding author at: 142 Haichuan Rd., Nanzih, 811 Kaohsiung, Taiwan, ROC. Tel.: +886 73617141x3218; fax: +886 75716013.

E-mail address: krwu@mail.nkmu.edu.tw (K.-R. Wu).

substrates reportedly exhibit a (0 0 1) preferential orientation [18]. The well-crystallized anatase facilitates the transfer of photo-generated electrons from bulk to surface, reducing the probability of recombination with holes, increasing both PC activity [16,17] and energy conversion efficiency [18]. Conducting $\text{SnO}_2\text{-F}$ substrate has been reported to promote the anatase–rutile transition [19], since tin can be segregated close to the surface of the film [20]. Therefore, tin in the substrate may be important in the formation of the microstructure of the grown TiO_2 film.

ITO is an n-type conductive semiconductor which is obtained by Sn-doping indium oxide (In_2O_3) with a low resistivity of $1.0 \times 10^{-4} \Omega \text{ cm}$ [20]. The maximum solubility of Sn-atoms in the In_2O_3 lattice is 5–6 at.%. When the dopant exceeds the optimal, no more tin atoms can be embedded in the In_2O_3 lattice, and the resistivity increases. This increase may be caused by interstitial tin atoms in the lattice, acting as charged trapping centers for the electrons. A phase separation of small SnO_2 particles in the crystalline ITO host material may occur. Since both the electronegativities and the ionic radii of Ti and Sn ions are similar, the Sn ions can easily substitute for Ti ions in the TiO_2 lattice, forming a stable solid solution ($\text{Ti}_{1-x}\text{Sn}_x\text{O}_2$) [2,21,22]. An Sn concentration of $x \leq 0.23$ can be completely dispersed in the anatase crystallite as a solid solution and the anatase–rutile phase transition and the crystallinity of the TiO_2 films can be promoted [21,22]. Therefore, reduction–oxidation states will evolve regardless of whether Sn ions enter the structure of TiO_2 lattices. Under certain preparative conditions, Sn ions that permeate into the growing TiO_2 film form a $\text{Ti}_{1-x}\text{Sn}_x\text{O}_2$ layer [23], which both theoretically and experimentally increases PC capabilities, by lowering the electron–hole recombination rate because of the increase in the band gap and Fermi level of the $\text{Ti}_{1-x}\text{Sn}_x\text{O}_2$ phase [21,24].

The separation and recombination of photogenerated charge carriers are competitive processes. The PC reaction in a layered TiO_2 /ITO catalyst is therefore effective only when the photogenerated holes are trapped on the surfaces to generate hydroxyl radicals ($^{\bullet}\text{OH}$) and the electrons can be easily transported to the ITO substrate. In this case, the electrons that are accumulated in the ITO substrate can finally be captured by the photogenerated holes. To improve further the photocatalytic performance of TiO_2 , the recombination of photogenerated charge carriers must be reduced. From this perspective, the electron-transfer process is a crucial factor of the separation of the photogenerated electron–hole pairs, and so critically influences PC capabilities. The properties of a heterostructured TiO_2 /ITO film cannot be considered solely as a simple combination of the properties of each component: atomic interactions and/or interdiffusion within the heterostructures must also be considered. Although many studies have elucidated the microstructural and PC properties of TiO_2 films grown on ITO substrates via various preparation techniques, the effect of interfacial properties of layered TiO_2 /ITO films on its properties has not been examined thoroughly to determine whether the Schottky barrier or third phase $\text{Ti}_{1-x}\text{Sn}_x\text{O}_2$ layer forms [9,10,16–18].

In this study, heterostructured TiO_2 /ITO catalysts with strong PC activity are prepared for potential industrial applications. The effect of the *in situ* sputtered ITO (sITO) on the PC properties is particularly important to explain the microstructures in detail. This study demonstrates that, in addition to the surface states and microstructures, the interfacial characteristics of the layered TiO_2 /ITO films critically affect both PC oxidation and reduction reactions.

2. Experimental procedure

2.1. Sample preparation

An in-house closed-field unbalanced magnetron sputtering system ($550^{\Phi} \times 600 \text{ mm}$, MIRDC, Taiwan) was used for sample

Table 1
Structural constituents of the layered samples used in this study.

Sample	Layer constituent	Deposition period (h)	Layer thickness (μm)
T(3)/sI	TiO_2/sITO	3.0/0.2	1.7/0.2
T(3)/al	TiO_2	3.0	1.6
T(3/3)/sI	$\text{TiO}_2/\text{TiO}_2/\text{sITO}$	3.0/3.0/0.2	1.4/1.6/0.2
T(6)/al	TiO_2	6.0	2.4
T(6)/sI	TiO_2/sITO	6.0/0.2	2.3/0.2
mT(6)/sI	$\text{TiO}_2/\text{sITO}/\text{TiO}_2/$ $\text{sITO}/\text{TiO}_2/\text{sITO}$	2.2/0.2/0.8/ 0.2/2.6/0.2	1.1/0.2/0.5/0.2/ 1.2/0.2

preparation. This study investigated the TiO_2 /ITO interfacial effect on the PC properties by preparing films with six heterostructures—two simplex, three duplex and one multi-stacked TiO_2 /ITO. Table 1 presents in detail the structural constituents and thicknesses of the layered samples. First, sITO thin films were initially deposited onto two sets of as-received ITO/glass (aITO, $17 \Omega/\text{sq}$. and $100 \pm 10 \text{ nm}$ thick) substrates using ITO targets (90 wt.% In_2O_3 and 10 wt.% SnO_2). The substrate holder was then rotated toward the titanium targets (99.95% purity) to form the TiO_2 film on the top of the sITO substrates. After the duration of 3.0 h, the sputtering chamber was opened to remove one set of TiO_2/sITO films, denoted T(3)/sI. Meanwhile, another set of aITO substrates was set immediately on the substrate holder where sample T(3)/sI had been fixed previously. The other set of TiO_2/sITO films remained in the chamber, and on the newly installed aITO substrates was deposited another TiO_2 film. The films were denoted T(3/3)/sI and T(3)/al, respectively. Therefore, sample T(3/3)/sI was prepared in an interrupted two-step deposition process to compare the effects of the successive one-step method on the microstructural and PC properties. To understand better tin diffusion, multi-stacked catalysts, mT(6)/sI, were prepared such that the deposition sequence was applied three times without opening the sputtering chamber. Finally, for comparison, another two duplex sets of TiO_2/sITO and TiO_2 films, denoted T(6)/sI and T(6)/al respectively, were prepared with twice the duration of deposition used for the T(3)/sI and T(3)/al films. Numbers 3 and 6 in the aforementioned sample notation represent total deposition durations of 3 and 6 h, respectively. A sputtering current of 1.0 and 3.2–3.4 A was applied to deposit ITO and TiO_2 films, respectively. All samples were deposited on aITO substrates under the same sputtering conditions without additional heating during deposition, except where otherwise stated.

2.2. Sample characterization

The layered TiO_2 /ITO samples were investigated using secondary ion mass spectrometer (SIMS, Cameca IMS-6f) for detail analysis of elemental relationship between the growing TiO_2 and ITO substrate. The crystal structures of the samples were analyzed by high-resolution X-ray diffractometer (XRD, Rigaku ATX-E) operating with $\text{Cu K}\alpha$ radiation. The (1 0 1) and (2 1 1) diffraction peaks were selected to determine the cell volumes of the anatase lattice parameters of samples. The mass fraction of rutile was estimated using the formula presented in Refs. [25–27]. The topography of each sample was analyzed using an atomic force microscope (AFM, SPI 3800N, Seiko Instruments) with a scan resolution of 512×512 pixels. Root mean square (RMS) and specific surface area ratio were estimated on an area of $1 \mu\text{m} \times 1 \mu\text{m}$. A scanning electron microscope (SEM, JEOL JSM-5400) and a high-resolution transmission electron microscope (HRTEM, Philips Tecnai 20, operated at 200 kV) were employed for microstructure characterization and composition analysis, both of which were equipped with an energy dispersive spectrometer (EDS). Lattice imaging coupled with two-dimensional Fourier transform and inverse transform were used to analyze the crystal structure of the selected samples. The d-spacings obtained from selective area electron diffraction (SAED) patterns

were used for least-squares refinement of the lattice parameters to analyze ion different effect.

2.3. Evaluation of photocatalytic and photoelectrochemical activities

The photocatalytic activity of the samples was evaluated by immersing samples with a size of 25 mm × 65 mm into 30 mL aqueous methylene blue (MB) solution pH (6.8) with an initial concentration of 10 mg/L (C_0). Prior to the PC test, the samples were soaked in the aqueous MB solution in darkness for equilibrium surface adsorption. The transmittance of the degraded MB solution was measured by a Shimadzu UV-1601 spectrometer at a wavelength of 664 nm. All experiments without stirring were performed under UV-light irradiation (UV-365, 3.5 mW/cm²) at about 25 °C. The blank experiments were performed under the identical conditions, but a glass slide or ITO glass substrate was used instead of a TiO₂/ITO film. The reaction rate constant was determined from the linear fitting of $\ln(C/C_0)$ as a function of reaction time (t), where C is the residual concentration of MB in the degraded MB solution. The reaction times were set at 1 h intervals from 1 to 5 h.

Forming •OH on photocatalyst surfaces has been considered as a main reaction mechanism for fast decomposition of various organic compounds in PC oxidation reactions [1]. Accordingly, the formation concentrations of these radicals can indicate the activities of catalyst in PC reactions. A convenient technique in terms of a radical scavenging method which uses radical sensitive species as radical captures was applied in this research for quantifying radical formation concentrations [17]. As an efficient scavenger for •OH, dimethyl sulfoxide (DMSO) was used to react with the radicals forming the TiO₂ films. DMSO can react with hydroxyl radicals to generate formaldehyde (HCHO) as a major reaction intermediate before complete mineralization. As a result, HCHO initial formation rates were measured for further determining radical formation concentrations on the TiO₂ catalysts. The HCHO initial formation rate is proportional to the radical formation concentration as DMSO can react with most of the radicals, theoretically. To determine HCHO concentration in solution in the study, a high performance liquid-phase chromatography (HPLC, Hitachi Inc., L-7455) with a fluorescent detector was applied. Before quantifying HCHO concentration with the HPLC, these HCHO-containing samples (2 mL) were mixed with 2.0-mL NH₃ and 0.5-mL 1,3-cyclohexanedione (CHD, 0.46 mM) in tubes to form fluoresce sensitive mixtures. These mixtures were further analyzed with the HPLC after being heated for 60 min. The operating conditions of the HPLC for HCHO quantification were summarized as follows: separation column was Mightysil RP-18 (Supelco, 25 cm × 4.6 mm, particle size 5 µm), liquid phase (methanol:water = 60:40 (v/v)), flow rate was set at 1.0 mL/min isocratic, and measurement wavelength of the fluoresce detector was set at 400 and 452 nm, respectively. HCHO calibration standards were purchased from Supelco.

The PEC tests were carried out with a standard PEC three-cell system that included a sample film anode with a working area of 20 mm × 50 mm, a saturated calomel electrode (SCE) reference electrode and a Pt wire counter electrode in a 4.0N Na₂CO₃ solution (pH ~ 11) via a potentiostat (CHI 610C, CH Instruments, Inc.). The Na₂CO₃ solution was purged with pure N₂ gas for 10 min to remove dissolved oxygen from the solution before testing, and was continuously stirred with a magnetic stirrer during the tests. The photocurrent was monitored as the catalyst anode was irradiated by UV lamps (2.7 mW/cm²). All of the chemicals were of analytical grade and the electrolyte was prepared with deionized distilled water. Hydrogen yield rates were determined by analyzing the gas that was liberated over the Pt cathode using gas chromatography (GC/TCD, HP4890).

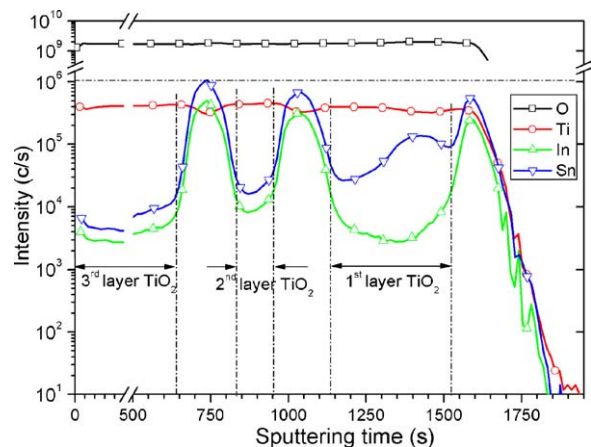


Fig. 1. Qualitative SIMS elemental depth profiles of mT(6)/sl sample.

3. Results and discussion

3.1. Qualitative SIMS elemental depth profiles

The diffusion of substrate species, such as Na and Si in the glass substrate, into the lattice of the growing TiO₂ film is a well-known phenomenon in the deposition of TiO₂ films. Since the exact nature of the final interface was dominated by the energy that was deposited by the ions and the chemical interaction between the affected elements, SIMS depth profiles were obtained to determine the qualitative composition of the layered TiO₂/ITO films. Figs. 1 and 2 present representative SIMS elemental depth profiles of the multi-stacked mT(6)/sl and T(6)/al catalysts, respectively. The mT(6)/sl interface between the sITO and the TiO₂ films was not sharp, indicating that substantial ionic diffusion occurred between layers. More tin diffused into the first grown TiO₂ film from the first sITO thin film (measured from the substrate) than into the second grown TiO₂ film from the second sITO thin film during deposition. Additionally, the tin intensity in the first layer of TiO₂ markedly exceeded that in the third layer, while indium intensity was about the same magnitude in the two layers. The tin intensity in the first sITO thin film was clearly lower than that in the second and third sITO layers. The tin intensity profile in the third layer was skewed toward the film surface, indicating that more tin diffusion occurred there, which situation contrasts with the approximately uniform tin intensity across the entire thickness of the T(6)/al sample in Fig. 2. Notably, tin permeated into the overlaying TiO₂ layer, but indium diffusion seemed to be negligible.

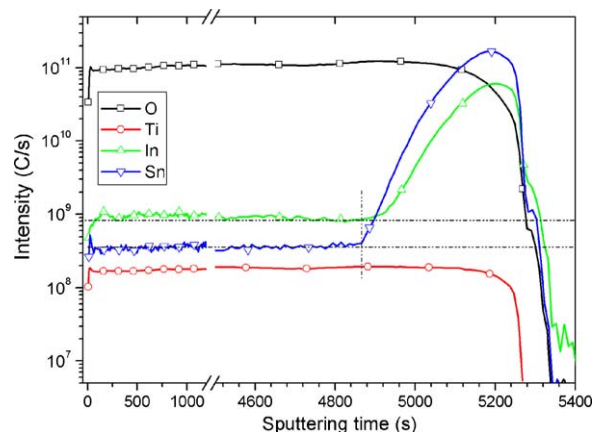


Fig. 2. Qualitative SIMS elemental depth profiles of T(6)/al sample.

Tin diffusion seemed to be negligible at the TiO_2/alTO interface in the T(6)/al sample, as presented in Fig. 2. Thus, the growth mechanism of the layered TiO_2/sITO films involves extensive tin diffusion into the lattice of the growing TiO_2 film from the sITO thin film, although Ti diffusion into the ITO may also be expected to increase slightly its electrical conductivity [28]. Therefore, tin diffusion was driven by the prolonged deposition of the overlaying TiO_2 film on the *in situ* sputtered ITO thin film that was freshly deposited under appropriate sputtering conditions, as revealed by the qualitative SIMS depth profiles of Fig. 1. This fact demonstrates that Sn-doped TiO_2 ($\text{Ti}_{1-x}\text{Sn}_x\text{O}_2$) layers may have formed at the interfaces of the TiO_2 and sITO thin films. Furthermore, the SIMS depth elemental profile revealed that a composition gradient of tin was observed in the first layer of the mT(6)/sl sample. Hence, a layered TiO_2/ITO catalyst with a declining bandgap towards to the film surface could be prepared by depositing the TiO_2 film on the sITO thin film by DC magnetron sputtering without post-heat treatment. Conversely, tin diffusion was suppressed by the third phase oxide or surface contaminants on the as-received ITO substrate, as was elucidated further using the following TEM images.

3.2. TEM observations

Dense, large columnar crystals with amorphous TiO_2 zones (>100 nm) are typically grown on an unheated glass substrate by reactive pulse magnetron sputtering or on a 600 °C-heated quartz substrate by r.f. sputtering [29,30]. These amorphous TiO_2 zones, inevitably formed above the inert substrates or a third phase likely produced at the heterostructured interface produced by two-step sputtering, reportedly inhibits PC activity [7,29]. In this work, however, an *in situ* sputtered ITO thin film substantially promotes the nucleation of the grown TiO_2 film.

Fig. 3 presents a cross-sectional TEM image of the first TiO_2/sITO interface of multi-stacked mT(6)/sl. It indicates that the growth of the first TiO_2 film started as a very thin amorphous layer. Interestingly, a crystalline TiO_2 layer with a thickness of about 50 nm is clearly observed to have grown on top of the thin amorphous layer. These crystallites formed the new $\text{Ti}_{1-x}\text{Sn}_x\text{O}_2$ layer, in a process that was promoted by the diffusion of tin from the sITO thin film. Thereafter, an amorphous TiO_2 zone extended to hundreds of nanometers from the $\text{Ti}_{1-x}\text{Sn}_x\text{O}_2$ layer before large

columnar TiO_2 crystals could dominate toward the second sITO thin film (not shown). The second TiO_2 layer nucleated immediately on top of the second sITO thin film without a notable amorphous thin layer. Well-crystallized TiO_2 films were fully formed at the third TiO_2/ITO interface (not shown).

Conversely, in a duplex T(6)/sl that was prepared with an extended deposition duration, the thickness of the amorphous TiO_2 layer was drastically reduced to several tens of nanometers, and the crystallinity of the anatase TiO_2 film was significantly increased. In fact, the newly formed $\text{Ti}_{1-x}\text{Sn}_x\text{O}_2$ layer crystallized further to a thickness of about 250 nm (not shown). These findings confirmed that, as well as an appropriate substrate temperature and the energy of impinging particles, a conductive ITO substrate promotes the crystallinity of the TiO_2 film prepared by DC magnetron sputtering even without additional heating. Anatase TiO_2 reportedly has the highest PC activity of all TiO_2 polymorphs [31]. A more amorphous grown TiO_2 film is known to exhibit less solar energy conversion efficiency and poor PC activity [32,33]. Hence, the well-crystallized anatase TiO_2 with the minimized proportion of amorphous phase has the best PC properties of any of the layered TiO_2/ITO catalysts.

The microstructure and surface morphology, developed during the growth of the film by magnetron sputtering, are controlled mainly by the energy of the depositing particles. The collision of ions dissipates thermal energy in the chamber and those ions that reach the substrate dissipate thermal energy into the substrate. The effect of energetic ions from the sputter plasma during extended deposition may compensate for the lack of thermal energy of the unheated substrate, and promote the crystalline growth of TiO_2 and sITO films. The differences between the amorphous thicknesses of the multi-stacked mT(6)/sl and duplex T(6)/sl films is explained by the effect of the thermal energy in the substrate as the deposition proceeds. In the deposition of the mT(6)/sl film, the thermal energy sharply fell as the sputtering current was reduced from 3.2 to 1.0 A as the deposition of the second *in situ* ITO thin film began. However, the deposition of the T(6)/sl films was continued at a sputtering current of 3.2–3.4 A without interruption until the end of the desired period. Additionally, an interrupted two-step deposition process was used to prepare the T(3/3)/sl sample. The TEM images revealed that an additional amorphous TiO_2 layer or third phase formed at the surface, and that TiO_2 crystal growth was interrupted when the second step of the deposition was resumed (not shown).

During the extended deposition of the TiO_2 film, Sn ion (0.71 Å) that diffused from the sITO thin film substituted for Ti ions (0.68 Å) in the growing TiO_2 lattice. The diffusion of Sn ions from the ITO thin film produced a $\text{Ti}_{1-x}\text{Sn}_x\text{O}_2$ thin film, reportedly increasing the oxidation–reduction potentials [21,24], and therefore the PC activity of the TiO_2 catalyst under UV illumination.

In this work, the concentration gradient of the Sn-element across the TiO_2/sITO and TiO_2/alTO interfaces was also evidenced by TEM-EDS. Table 2 presents the Sn concentrations in positions that correspond to the numbers marked in the TEM image in Fig. 3. For sample mT(6)/sl, positions I1 and i1 at the very bottom of the sITO thin film exhibited a slightly low Sn/In atomic ratio of

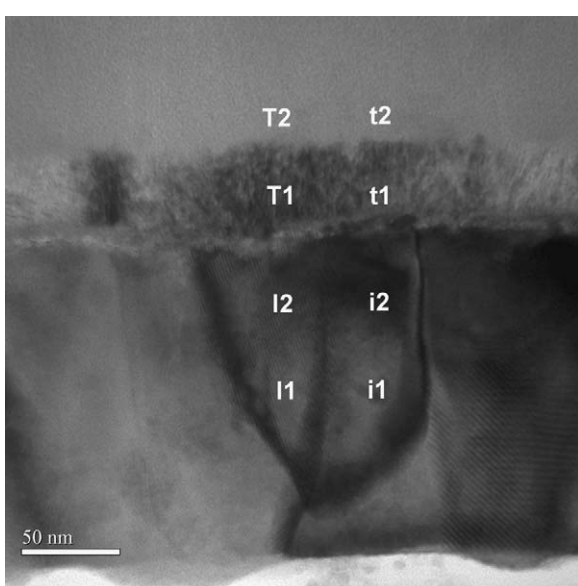


Fig. 3. Detailed cross-sectional TEM image of mT(6)/sl sample at the first TiO_2/sITO interface.

Table 2

Sn concentrations in areas that correspond to the numbers in the TEM images in Figs. 3 and 4.

Sample	Position							
	Sn/In (at.%)				Sn/(O ₂ +Ti+In) (at.%)			
	I1	I2	i1	i2	T1	T2	t1	t2
mT(6)/sl	7.3	5.3	7.1	6.4	4.7	~0.0	5.7	~0.0
T(6)/al	11.9	12.2	12.6	12.1	~0.0	~0.0	~0.0	~0.0

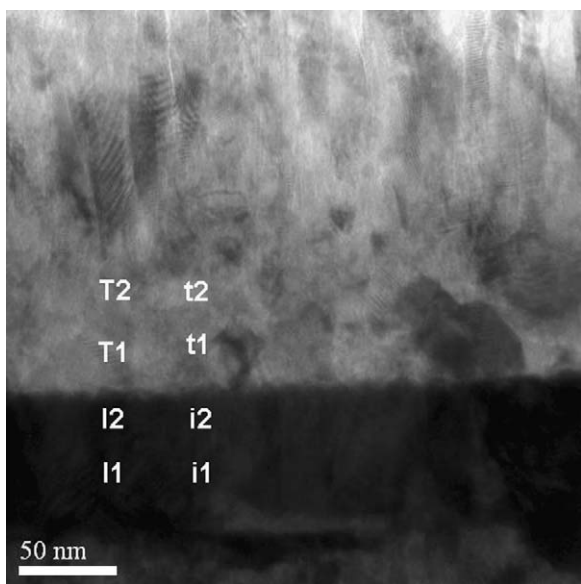


Fig. 4. Detailed cross-sectional TEM image of T(6)/al sample at the TiO_2/alTO interface.

7.3 and 7.1 at.%, respectively. Positions I2 and i2 close to the TiO_2/sITO interface had a smaller Sn/In ratio of 5.3 and 6.4 at.%, respectively. At positions T1 and t1 in the TiO_2 film, the Sn contents were relatively high (4.7 and 5.7 at.%), whereas at positions T2 and t2, tin was entirely undetectable. When a high sputtering power was maintained for a long period, the decline in the tin concentration as the substrate temperature increased was considered to increase the segregation of tin at the surface of the ITO lattices [34]. These results verify that tin in the sITO really diffused into the growing TiO_2 film during the deposition process. Tin diffusion was weaker at the second and the third TiO_2/sITO interfaces in sample mT(6)/sI (not shown). This result is explained by the fact that the second and third TiO_2 films were deposited with a shorter deposition period.

At the corresponding positions on sample T(6)/al, marked in Fig. 4, the alTO thin film had a typical Sn/In ratio (11.9–12.1 at.%) and the overlaying TiO_2 film had an undetectable Sn concentration. Barely any diffusion was observed at the TiO_2/alTO interface in sample T(6)/al. These findings are consistent with the qualitative SIMS analyses in Section 3.1.

These findings were further analyzed by measuring the d-spacings of the first TiO_2/sITO interfaces of sample mT(6)/sI via HRTEM images and SAED patterns. Fig. 5 shows a characteristic HRTEM lattice image of the first TiO_2/sITO interface along with the Fourier transform and reconstructed images corresponding to the microstructures marked with squares (I), (II) and (III). Interplanar spacings and angles observed in Fig. 5(b) correspond to a microstructure with anatase phase oriented along the $[1\ 0\ 0]$ zone axis of the Sn-doped anatase TiO_2 layer. The reconstructed image displayed in Fig. 5(c) could be interpreted as a defect-free anatase TiO_2 . The least-squares refinement of the d-spacing of the Sn-doped TiO_2 indicated that the dissolution of large-sized Sn cation caused minor change of the anatase lattice parameters ($a = 3.789 \text{ \AA}$, $c = 9.609 \text{ \AA}$, and cell volume = 137.95 \AA^3) in comparison with the undoped anatase TiO_2 ($a = 3.7852 \text{ \AA}$, $c = 9.5139 \text{ \AA}$ and cell volume = 136.31 \AA^3 JCPDS file 21-1272). Fourier transform and reconstructed image of the amorphous TiO_2 layer in the marked square (II) was displayed in Fig. 5(d) and (e), respectively. Moreover, Fig. 5(f) and (g) shows the Fourier transform and reconstructed image of the first sITO matrix in the marked square (III), respectively. The ITO matrix has facet parallel to $(2\ 2\ 2)$ as

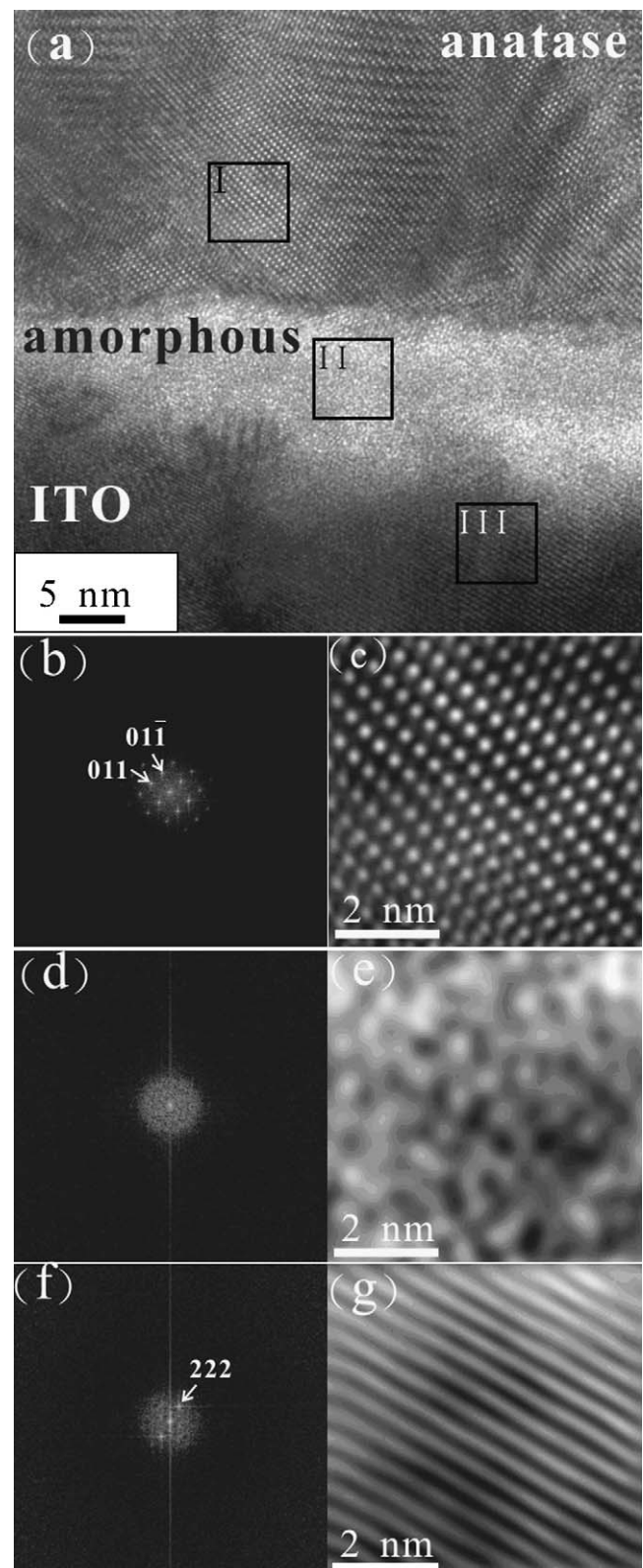


Fig. 5. (a) Cross-sectional lattice image of the first TiO_2/sITO interface of sample mT(6)/sI with marked squares (I), (II) and (III); (b and c) Fourier transform along the $[1\ 0\ 0]$ zone axis and the reconstructed image of the Sn-doped anatase layer in the marked square (I); (d and e) Fourier transform and reconstructed image of the amorphous TiO_2 layer in the marked square (II); (f and g) Fourier transform and reconstructed image of the first sITO matrix in the marked square (III), respectively.

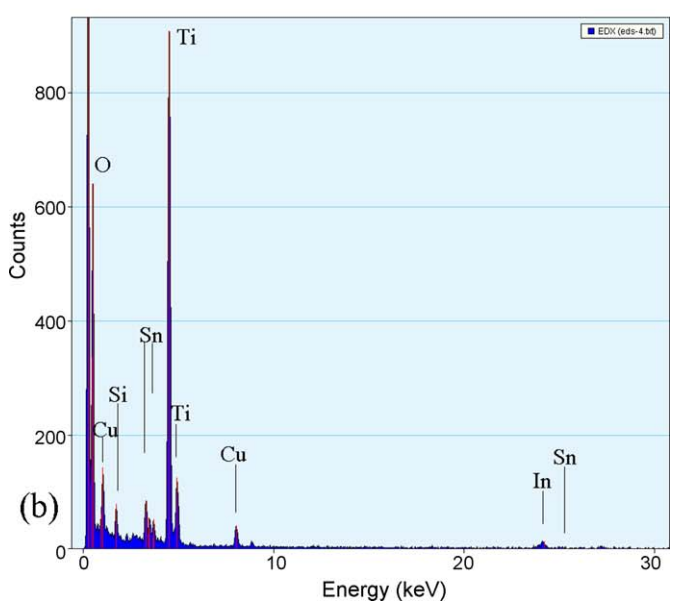
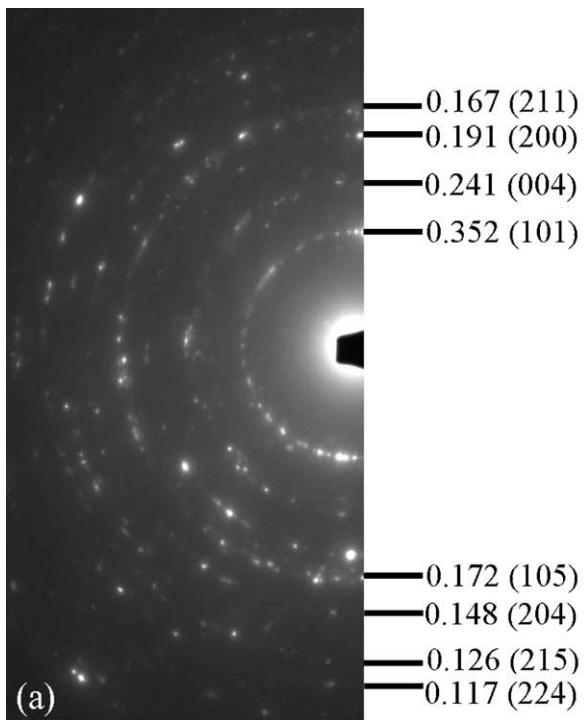


Fig. 6. (a) TEM SAED pattern of Sn-doped anatase TiO_2 layer in random orientation; (b) EDS spectrum of TiO_2 layer showing diffused Sn element in the growing TiO_2 layer.

indicated by the lattice image (Fig. 5(a)), two-dimensional Fourier transform (Fig. 5(f)) and inverse transform (Fig. 5(g)) of the ITO matrix.

Fig. 6(a) shows the SAED pattern of the Sn-doped anatase TiO_2 layer in random orientation. The indexed diffraction peaks agreed with the typical values of polycrystalline anatase TiO_2 . The d-spacings of sample mT(6)/sl obtained from the SAED pattern were compared with those of bulk values for anatase. All the obtained d-spacings (Fig. 6(a)) were a little larger than those of bulk ones [2], which implied that tin substituted for Ti ions in the TiO_2 lattice, leading to an expansion of the TiO_2 lattice. As displayed in Fig. 6(b), the EDS spectrum of the marked square (I) in Fig. 5(a) reveals the possible existence of Sn element in the growing TiO_2 film.

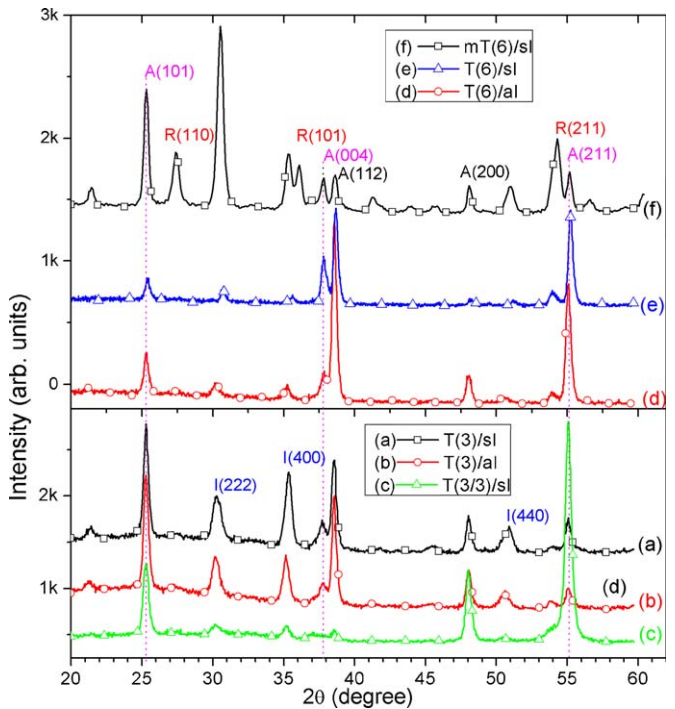


Fig. 7. XRD patterns of all six samples: (a) $\text{T}(3)/\text{sl}$, (b) $\text{T}(3)/\text{al}$, (c) $\text{T}(3/3)/\text{sl}$, (d) $\text{T}(6)/\text{al}$, (e) $\text{T}(6)/\text{sl}$ and (f) $\text{mT}(6)/\text{sl}$.

3.3. XRD, UV-vis, SEM and AFM analyses

Fig. 7 presents the XRD patterns of all six samples—two simplex samples, $\text{T}(3)/\text{sl}$ and $\text{T}(3)/\text{al}$, three duplex samples, $\text{T}(3/3)/\text{sl}$, $\text{T}(6)/\text{sl}$ and $\text{T}(6)/\text{al}$ and one multi-stacked sample, $\text{mT}(6)/\text{sl}$. Samples $\text{T}(3)/\text{sl}$ and $\text{T}(3)/\text{al}$ exhibited the typical anatase TiO_2 phase and had very similar diffraction patterns, as presented in Fig. 7(a) and (b). Fig. 7(c)–(e) indicates that the $(2\bar{1}\bar{1})/(1\bar{0}1)$ intensity ratio of samples $\text{T}(3/3)/\text{sl}$, $\text{T}(6)/\text{sl}$ and $\text{T}(6)/\text{al}$ increased significantly from a typical value of 0.2 to a relatively high ratio of 3.1–4.5. As indicated in Table 3, sample $\text{T}(3/3)/\text{sl}$ had the lowest $(0\bar{0}4)/(1\bar{0}1)$ intensity ratio of 0.07 and sample $\text{T}(6)/\text{sl}$ had the highest, 2.21, of the six samples. A remarkable increase in the PC and PEC performance has been reported for the $(0\bar{0}1)$ -oriented diffraction from TiO_2 nanocrystalline films [18] and anatase TiO_2 single crystals [35,36]. It is attributed to their differences in crystallinity and crystal orientation, as well as the more negative flatband potential of the $(0\bar{0}1)$ plane. Therefore, the high crystallinity with the preferred $(0\bar{0}1)$ plane of the TiO_2 film promotes the separation of the photogenerated electrons and holes. The diminishment of the $(0\bar{0}4)$ peak of sample $\text{T}(3/3)/\text{sl}$ was possibly associated with the formation of an amorphous layer by the interrupted two-step deposition process, which was also one of the causes of the difference between the PEC and PC performances of the samples.

The multi-stacked film, $\text{mT}(6)/\text{sl}$, exhibited a prevalent rutile TiO_2 structure with a mass fraction of about 36.0%, as shown in Table 3. And, an anatase phase whose $(2\bar{1}\bar{1})/(1\bar{0}1)$ and $(0\bar{0}4)/(1\bar{0}1)$ intensity ratios typically remained 0.33 and 0.28, respectively, as presented in Fig. 7(f) and Table 3. However, no such rutile phase was observed in other samples. Pure rutile TiO_2 typically begins to form at about 700 °C [37]. These results verify that Sn-doping promotes the anatase–rutile phase transition [21,22,26–28], but do not alter the surface energy of the TiO_2 crystal in the growth of the reactive $\{0\bar{0}1\}$ facets. The tin diffusion was very extensive at the first TiO_2/ITO interface of the $\text{mT}(6)/\text{sl}$ film in which the embedded multi-layer sITO thin films were deposited

Table 3

Structural and surface properties of the samples.

Sample	XRD peak intensity ratio		Cell volume (Å ³)	Rutile mass fraction	Specific surface area ratio	RMS roughness (nm)
	(0 0 4)/(1 0 1)	(2 1 1)/(1 0 1)				
T(3)/sl	0.27	0.34	135.39	Trace	1.09	8.8
T(3)/al	0.18	0.18	134.95	Trace	1.06	8.3
T(3/3)/sl	0.07	3.14	136.56	Trace	1.11	9.9
T(6)/al	0.68	3.10	136.50	Trace	1.21	18.5
T(6)/sl	2.21	4.54	137.10	Trace	1.23	22.2
mT(6)/sl	0.28	0.33	137.68	36.0%	1.24	21.5

over an extended period. The formation of the $\text{Ti}_{1-x}\text{Sn}_x\text{O}_2$ layer can be tailored by, for example, adjusting the position of multi-stacked sITO thin films. As displayed in Table 3, a noticeable expansion of cell volume of 137.68 \AA^3 , compared with a typical value of 136.31 \AA^3 [2], was obtained for sample mT(6)/sl. This has been observed for the $\text{Ti}_{1-x}\text{Sn}_x\text{O}_2$ particles with a tin content of about 5–7 wt.% [25,27]. This indicated that the tin diffusion could substitute for Ti ions in the TiO_2 lattice, forming $\text{Ti}_{1-x}\text{Sn}_x\text{O}_2$ solid solution. The fact that no segregated SnO_2 phase was found at the diffraction peaks of 27° , 34° and 52° also conformed this finding [27]. The SIMS depth profiles in Fig. 1 also indicated that tin diffused from the sITO thin film into the growing TiO_2 film. Sample T(6)/sl also exhibited a slight expansion of cell volume of 137.10 \AA^3 , as listed in Table 3, implying a significant Sn-doping effect upon the growing TiO_2 film.

A significant increase in both (0 0 4)/(1 0 1) and (2 1 1)/(1 0 1) intensity ratios of samples T(6)/sl and T(6)/al may have been caused by crystal coarsening induced by the synergetic effect of the ITO substrate and an extended deposition period. Crystal coarsening, and the consequent growth of large grains, was driven by a drop in the surface energy under hydrothermal conditions [38,39]. Therefore, the percentage of reactive {0 0 1} facets increased, favoring the photoactivity of the TiO_2 films—in a manner consistent with the findings of Deng et al. [18]. This synergetic effect was not observed either on the glass substrate or in the carbon-free environment in a relative short period (data not shown). Restated, the ITO substrate was critical to the formation of a highly photocatalytic TiO_2 film under the prescribed conditions.

It is known that thicker films, subjected to longer heat treatment by repeated heating cycle or extended deposition duration, have relatively larger anatase crystallites and this causes the onset of absorption to shift to the red part of the spectrum

[10,40]. Additionally, the porous-structured films become highly light scattering [41,42]. Fig. 8 exhibits the UV-vis absorption spectra of all the six TiO_2 films. The variation between simplex samples, T(3)/al and T(3)/sl, and other four duplex samples, i.e. T(3/3)/sl, T(6)/sl, T(6)/al and mT(6)/sl, in UV-vis absorption spectra was mainly due to particle growth under extended deposition period. The visualized evidence for the particle growth of the films under extended deposition duration was obtained from SEM measurements which are illustrated in Fig. 9. Sample mT(6)/sl exhibited the least UV-vis absorption among four duplex samples whose TiO_2 thickness was the second largest at $2.8 \mu\text{m}$, as shown in Table 1. The blue shift of bandgap energy could happen in sample mT(6)/sl due to possibly the formation of $\text{Ti}_{1-x}\text{Sn}_x\text{O}_2$ layer and the rutile phase. $\text{Ti}_{1-x}\text{Sn}_x\text{O}_2$ that exhibited cell volume expansion has been reported to have a red shift of bandgap energy of 0.1–0.2 eV [25,27]. This indicated that Sn-doping could slightly increase the bandgap energy of the TiO_2 layer. Conversely, sample T(3)/sl and T(3)/al exhibited the same UV-vis absorption spectra, indicating no thick enough $\text{Ti}_{1-x}\text{Sn}_x\text{O}_2$ layer was formed in both samples. Note that most of the red shift of the bandgap energy and visible-light absorption of sample T(6)/sl could be ascribed, in part, to the light scattering effect [42,43]. The light scattering effect induced by the inherently columnar porous structure (TEM figure not shown) of DC magnetron sputtering technique reportedly benefits the light collection [10,19]. The photocatalytic activity could be enhanced [42].

Fig. 9 presents SEM surface morphologies of all six samples. Samples T(3)/sl, T(3)/al and T(3/3)/sl exhibited similar morphological patterns with dense, flat surfaces, although T(3/3)/sl had a slightly rougher surface than the other two, as shown in Fig. 9(a)–(c), respectively. Both samples T(6)/al and T(6)/sl had distinct morphological features with more nanoporous surfaces, as shown in Fig. 9(d) and (e). The nanoporous surface structures of these films, consistent with the AFM measurements that will be discussed in the next section, make them potentially effective catalysts. The multi-stacked mT(6)/sl film, presented in Fig. 9(f), had the most roughest surface of any of the six samples with symmetrical particles. Typical polygon-shaped rutile TiO_2 particles along with pyramidal particles of the anatase phase on the surface indicated the effects of sITO thin film on the formation of the TiO_2 microstructure and, thereby, the PC properties.

Table 3 presents the surface properties of the samples, estimated from AFM measurements. Samples mT(6)/sl, T(6)/al and mT(6)/sl had the highest specific surface area ratios of about 1.24 and an RMS of 18.5–21.5 nm. Accordingly, these films could absorb more incident photon energy and so exhibited greater PC activity. Declines in the surface roughness and specific surface area ratio were mostly associated with the decrease in the grain size caused by reducing the deposition period, as evidenced by the fact that samples T(3)/al and T(3)/sl had the lowest such values. The less porous morphology and smaller columnar crystals were observed in sample T(3/3)/sl because of the formation of an additional amorphous TiO_2 layer or third phase formed when the second-step deposition resumed.

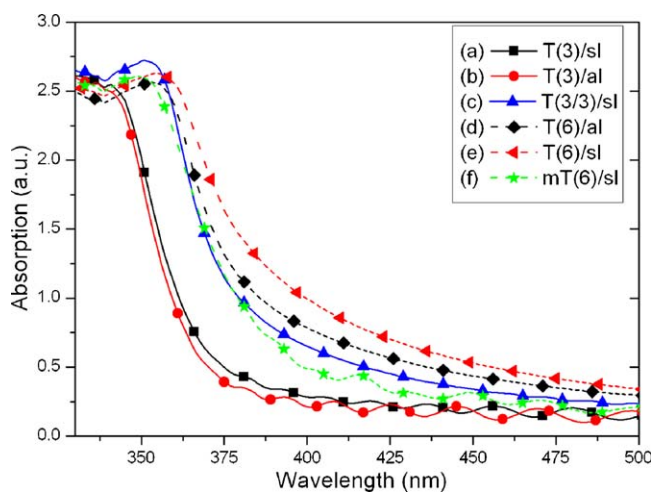


Fig. 8. UV-vis absorption spectra of all six samples: (a) T(3)/sl, (b) T(3)/al, (c) T(3/3)/sl, (d) T(6)/al, (e) T(6)/sl and (f) mT(6)/sl.

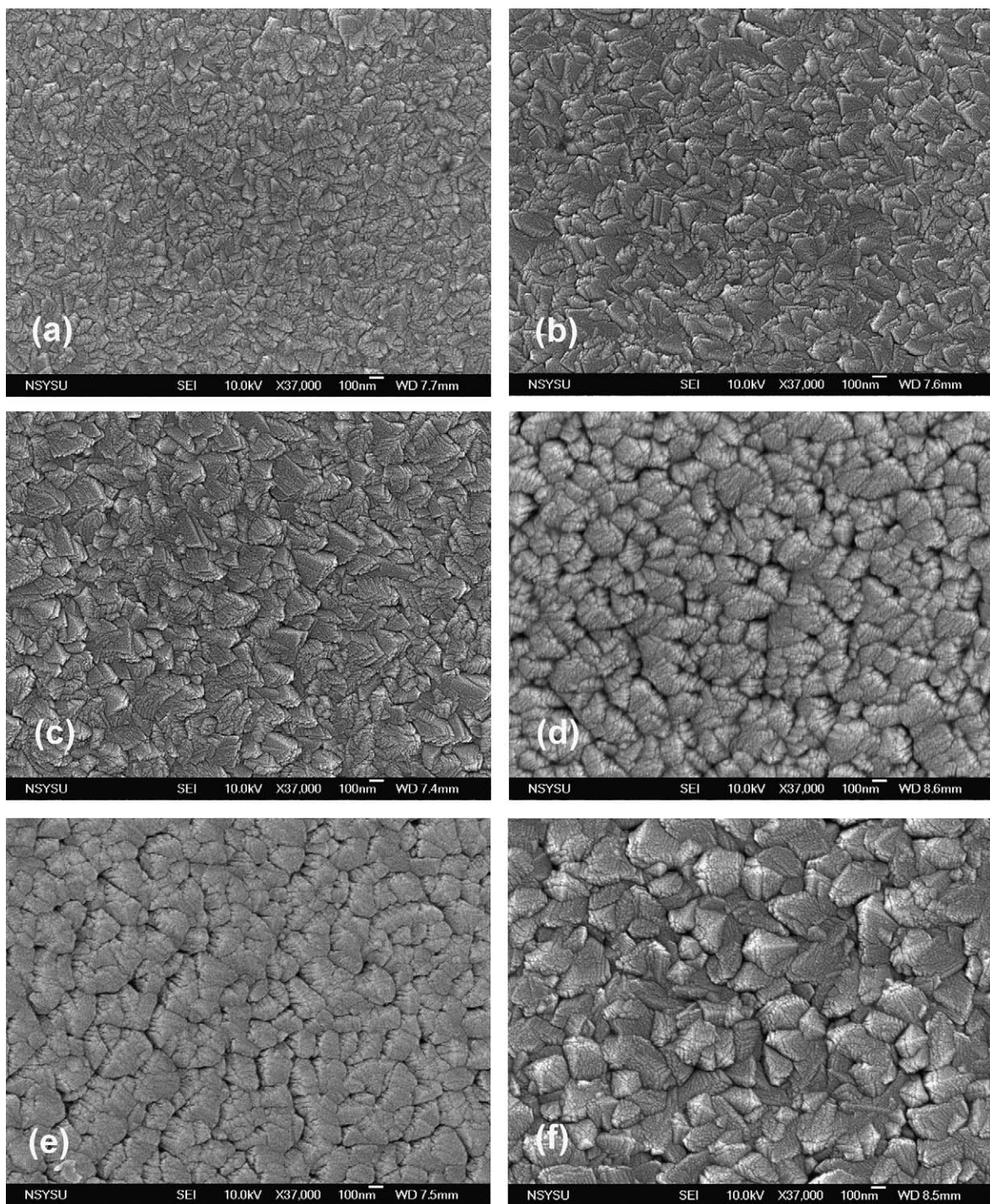


Fig. 9. SEM plain views of all six samples: (a) T(3)/sl, (b) T(3)/al, (c) T(3/3)/sl, (d) T(6)/al (e) T(6)/sl and (f) mT(6)/sl.

3.4. MB and DMSO oxidation tests

To investigate the effect of the sITO thin film on the PC capabilities of the layered TiO₂/ITO catalysts, the PC degradation of both MB and DMSO were performed. MB can be oxidized by an attack by •OH, and DMSO is an efficient radical scavenger of •OH [44]. Hydroxyl radicals, produced by the photogenerated holes, have been proposed as reactive species for the rapid decomposition of many organic compounds in liquid-phase PC reactions [1]. Thus, it is preferable that the photogenerated holes can be exposed to the film surface in contact with aqueous solution.

The PC activity of TiO₂ depends on many factors, including crystallinity, surface area, crystal orientation, surface hydroxyl density, phase composition and even thickness of TiO₂ films [19,35,36,45–47]. The high crystallinity of anatase TiO₂, for instance, is responsible for the high MB degradation rate [46,47]. Table 4 presents the first-order reaction rate constants (*k*) of MB, assisted by various TiO₂/ITO films. Sample T(6)/sl had the highest reaction rate constant *k* = 0.33 h⁻¹, whereas sample mT(6)/sl exhibited the second highest *k* = 0.25 h⁻¹ under UV-365 illumination. This result could be intuitively attributed to an increase in the bandgap energy and a high Fermi level energy of the

Table 4

MB degradation rate constant (k), hydroxyl radical concentration and photo-generated current density at 0.5 V vs. SEC under UV-365 irradiation.

Sample	MB reaction rate constant k (h^{-1})	Hydroxyl radical concentration ($\times 10^{-18} \text{ M}$)	Photocurrent density ($\mu\text{A}/\text{cm}^2$)
T(3)/sl	0.20	4.02	59
T(3)/al	0.12	3.47	106
T(3/3)/sl	0.11	3.34	31
T(6)/al	0.18	3.92	482
T(6)/sl	0.33	5.29	269
mT(6)/sl	0.25	5.17	90
Blank	0.03	—	—

$\text{Ti}_{1-x}\text{Sn}_x\text{O}_2$ layer formed in both samples. The highest rate constant of the former was beneficial more from the reactive sites of the (0 0 1) plane since both samples had nearly the same morphological and dimensional properties. Sample T(3/3)/sl had the lowest $k = 0.11 \text{ h}^{-1}$ which was reportedly resulted from the fast recombination of electron–hole pairs in the amorphous TiO_2 zone [33]. Sample T(6)/al had a slightly lower $k = 0.18 \text{ h}^{-1}$ than sample T(3)/sl, $k = 0.20 \text{ h}^{-1}$, although it contained a highly crystalline anatase TiO_2 phase with reactive sites of the (0 0 1) plane. This may have resulted partially from the formation of the Schottky barrier without an oxidation-rich $\text{Ti}_{1-x}\text{Sn}_x\text{O}_2$ layer in sample T(6)/al.

In general, photocatalytic activity is closely related with the lifetime of photogenerated electrons and holes. A Schottky barrier can form at the TiO_2/ITO interface since ITO has a higher work function than TiO_2 . The height of the Schottky barrier, Φ_b , is related to the work function (Φ_m) of ITO, which is given by $\Phi_b = \Phi_m - E_x$, where E_x is the electron affinity, measured from the conduction band edge to the vacuum level of TiO_2 catalyst [9]. The work function of $\text{Ti}_{1-x}\text{Sn}_x\text{O}_2$ is presumably a bit higher than that of the host TiO_2 but lower than that of the ITO substrate, provided that the bandgap energy is slightly increased due to Sn-doping [25,27]. The Schottky barrier remained effectively. Thus, the photogenerated electrons could continuously transfer across the $\text{TiO}_2/\text{Ti}_{1-x}\text{Sn}_x\text{O}_2/\text{ITO}$ interface to ITO substrate and thus recombination was effectively suppressed. A decrease in the electrical conductivity of the $\text{Ti}_{1-x}\text{Sn}_x\text{O}_2$ and ITO would not affect the PC activity in absence of an applied potential. However, under an anodic potential, it might have certain effect on photoelectrocatalytic activity [15]. The further investigation is needed.

3.5. Photocurrent measurements

In an irradiated TiO_2/ITO electrode under an applied potential, the photogenerated holes are separated from the electrons. Holes move to the semiconductor surface, where they are trapped or captured by the reduced species in the electrolyte. And, the electrons are transported to the high electrical conductivity ITO substrate where a Schottky barrier can form at the TiO_2/ITO interface. Since this process must overcome the internal resistance of the electrode, the higher the electrical conductivity the lower is the photocurrent loss is obtained. A lower sheet resistance substrate reportedly improves the photocurrent response of dye-sensitized solar cells [48]. Yu et al. have reported on the striking increase in photocurrent obtained from a TiO_2 electrode where a conductive TiC interlayer exists between TiO_2 and carbon nanotube. They have attributed the phenomenon to the conductive TiC which can facilitate electrons transport more freely to an external circuit and obtain an excess of photogenerated holes in the TiO_2 migrating to the surface [14]. Conversely, a drastic decrease in photocurrent has reported on the Cr-doped TiO_2 electrode due to its lower electrical conductivity [5].

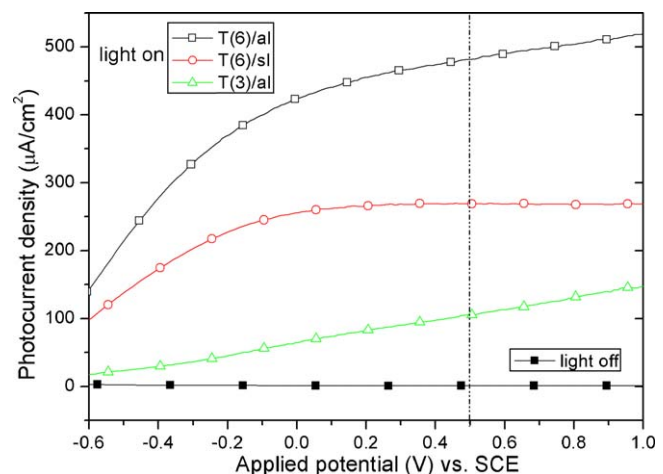


Fig. 10. Representative I - V characteristics of T(3)/al, T(6)/al and T(6)/sl electrodes under UV-365 irradiation.

The magnitude of the generated anodic photocurrent upon irradiation of the electrodes in the PEC cell corresponds to the charge separation efficiency of the electrode. Fig. 10 plots the I - V characteristics of T(3)/sl, T(6)/al and T(6)/sl film electrodes in 4N Na_2CO_3 electrolyte under UV-365 irradiation. The photocurrent density of sample T(6)/al increased bilinearly with the applied potential—more steeply at the negative potential and more slowly at positive. The first fast increase in photocurrent density was associated with the formation of the Schottky barrier at the TiO_2/alTO interface, because the Schottky barrier enhanced the transfer of photogenerated electrons from the TiO_2 film to the alTO substrate, promoting the generation of photocurrent [9]. Further increasing the applied potential reduced the driving force of the separation of the photogenerated holes and electrons by thinning the space charge layer in sample T(6)/al. However, the Schottky barrier may have disappeared because of the formation of a $\text{Ti}_{1-x}\text{Sn}_x\text{O}_2$ layer at the TiO_2/sITO interface of sample T(6)/sl. Therefore, the photocurrent density of sample T(6)/sl increased linearly until reaching its plateau of $269 \mu\text{A}/\text{cm}^2$ at $+0.15 \text{ V}$ vs. SCE.

The photocurrent density of sample T(3)/sl increased linearly throughout the range of applied potentials, but with the lowest gradient, at least in part because of thinness of the film and the existence of a thin Schottky barrier. A thin film of various catalysts was not sufficiently thick to absorb the entire incident light [45,49,50]. A thin Schottky barrier weakly drives the separation of the photogenerated holes and electrons. As presented in Table 4, sample T(6)/sl, with about the same thickness, $2.3 \mu\text{m}$, as T(6)/al, had the second highest photocurrent density of the six electrodes, $269 \mu\text{A}/\text{cm}^2$, but only 56% of that of the T(6)/al electrode ($482 \mu\text{A}/\text{cm}^2$) at an applied potential of $+0.5 \text{ V}$ vs. SCE. Electron transport in sample T(6)/al was easily facilitated using an alTO thin film in which no tin diffusion was expected.

A rather poor photocurrent response and the low density in sample T(6)/sl may have resulted from the $\text{Ti}_{1-x}\text{Sn}_x\text{O}_2$ layer, in which a decline in the electrical conductivity for $x < 0.1$ has been reported upon [51]. More importantly, the resistivity can be increased by a factor of eight by reducing the Sn content in the sITO thin film [52]. High electrical conductivity facilitates the separation of photogenerated electrons and holes, preserving the photocurrents of the electrodes [53,54]. Therefore, the increase in electrical resistance can adversely affect the photogenerated electrons in the PEC cell, reducing the photocurrent, because a PEC electrode should be barrier free, enabling electrons to be transported rapidly without loss of energy. The photocurrent densities of samples T(3/3)/sl and T(3)/sl were the lowest, perhaps in part

because of the thinness of the T(3)/sI film and a large amorphous TiO₂ zone in the T(3/3)/sI electrode.

4. Conclusion

The elemental composition of multi-stacked mT(6)/sI and duplex T(6)/al film, and the microstructural properties of the same mT(6)/sI and T(6)/al films, along with T(6)/sI and T(3/3)/sI films, were examined by SIMS and TEM, respectively. The formation of a Ti_{1-x}Sn_xO₂ layer was favored in the TiO₂/sITO junction, reducing the electron–hole recombination rate by increasing the band gap and Fermi level. The conductive ITO substrate substantially improved the crystallinity of the TiO₂ film, even without additional heating, upon DC magnetron sputtering. Two simplex T(3)/sI and T(3)/al films were examined using conventional methods. The XRD patterns of T(3)/sI, T(3)/al and T(3/3)/sI films revealed only the anatase TiO₂ phase and had very similar diffraction patterns. SEM measurements show that the three films appeared to have strikingly similar morphologies and lateral grain sizes. AFM measurements yielded similar findings to those obtained by SEM: the T(3)/sI T(3)/al and T(3/3)/sI films had similar phase compositions, crystallinities and surface morphology, but significantly differs PCs (MB and DMSO) and PEC activities. These differences were not solely attributable to the aforementioned characteristic bias. Notably, although sample T(3/3)/sI had a rougher surface and a thicker film, its reaction rate constant and photocurrent density were just over half of the T(3)/sI sample. It had about the same the reaction rate constant as sample T(3)/al, but only one third the photocurrent density. These findings follow from the fact that the Ti_{1-x}Sn_xO₂ phase in sample T(3)/sI increases the PC activities to approach that of the mT(6)/sI film. An increase in the reactive {0 0 1} facets of samples T(6)/sI and T(6)/al may have been caused by the synergistic effect of the conductive ITO substrate and an extended period of deposition. A thick film thickness resulted from an extended period of deposition using DC magnetron sputtering provides columnar porous structure which enhance light collection. A large increase in the electrical resistance of the sITO thin film may have slightly reduced the photocurrent density of sample T(6)/sI. Formation of the Schottky barrier in the TiO₂/alTO interface, as in T(6)/al, further increases the PEC activity, while the PC activities of the samples were equally efficient since a high percentage of the reactive sites remained active. Finally, low PC and PEC activities of sample T(3/3)/sI may be associated with the formation of a weakly active amorphous TiO₂ layer in the middle of the TiO₂ film in thickness direction, because of the two-step deposition of sample T(3/3)/sI.

In summary, in this work, reactive DC magnetron sputtering without additional substrate heating was adopted to sputter well-crystallized anatase TiO₂ films onto ITO substrates. The results show that the ITO substrate, either sputtered *in situ* or as-received, was key to tailoring the phase composition, crystal orientation, crystallinity and surface morphology of the growing TiO₂ films under a particular conditions. The results offer a foundation of further work to develop more efficient catalysts of the oxidation of hazardous chemicals and/or the PC reduction of spitting water for hydrogen production. This finding is critical to the potential deposition of layered TiO₂ catalysts on low-melting point substrates and for reducing the costs of production.

Acknowledgements

The financial support by National Science Council of Taiwan ROC under grant NSC 97-2221-E-022-007 is gratefully acknowledged. The authors wish to thank Mr. P.S. Hsu, Y.T. Su, L.H. Cheng and C.Y. Chung of National Kaohsiung Marine University for their sample preparations.

References

- [1] A. Fujishima, T.N. Rao, D.A. Tryk, *J. Photochem. Photobiol. C: Photochem. Rev.* 1 (2000) 1–21.
- [2] U. Diebold, *Surf. Sci. Rep.* 48 (2003) 53–229.
- [3] B. O'Regan, M. Grätzel, *Nature* 353 (1991) 737–739.
- [4] M. Ferroni, M.C. Carotta, V. Guidi, G. Martinelli, F. Ronconi, M. Sacerdoti, E. Traversa, *Sens. Actuators B: Chem.* 77 (2001) 163–166.
- [5] M. Radecka, M. Rekas, A. Trenczek-Zajac, K. Zakrzewska, *J. Power Sources* 181 (2008) 46–55.
- [6] Y. Cao, X. Zhang, W. Yang, H. Du, Y. Bai, T. Li, J. Yao, *Chem. Mater.* 12 (2000) 3445–3448.
- [7] H. Irie, H. Mori, K. Hashimoto, *Vacuum* 74 (2004) 625–629.
- [8] S. Higashimoto, M. Sakiyama, M. Azuma, *Thin Solid Films* 503 (2006) 201–206.
- [9] W. Dai, X. Wang, P. Liu, Y. Xu, G. Li, X. Fu, *J. Phys. Chem. B* 110 (2006) 13470–13476.
- [10] K.R. Wu, T.P. Cho, *Appl. Catal. B: Environ.* 80 (2008) 313–320.
- [11] M. Kitano, K. Tsujimaru, M. Anpo, *Appl. Catal. A: Gen.* 314 (2006) 179–183.
- [12] Y. Chen, J.C. Crittenden, S. Hackney, L. Sutter, D.W. Hand, *Environ. Sci. Technol.* 39 (2005) 1201–1208.
- [13] H. Chen, S. Chen, X. Quan, H. Yu, H. Zhao, Y. Zhang, *J. Phys. Chem. C* 112 (2008) 9285–9290.
- [14] H. Yu, X. Quan, S. Chen, H. Zhao, *J. Phys. Chem. C* 111 (2007) 12987–12991.
- [15] B. Gao, C. Peng, G.Z. Chen, G.L. Puma, *Appl. Catal. B: Environ.* 85 (2008) 17–23.
- [16] Y. Ma, J.B. Qiu, Y.A. Cao, Z.S. Quan, J.N. Yao, *Chemosphere* 44 (2001) 1087–1092.
- [17] D. Dumitriu, A.R. Bally, C. Ballif, P. Hones, P.E. Schmid, R. Sanjinés, F. Lévy, V.I. Părvulescu, *Appl. Catal. B: Environ.* 25 (2000) 83–92.
- [18] H. Deng, H. Zhang, Z. Lu, *Chem. Phys. Lett.* 363 (2002) 509–514.
- [19] J. Rodríguez, M. Gómez, S.-E. Lindquist, C.G. Granqvist, *Thin Solid Films* 360 (2000) 250–255.
- [20] N. Nadaud, N. Lequeux, M. Nanot, J. Jove, T. Roisnel, *J. Solid State Chem.* 135 (1998) 140–148.
- [21] S. Mahanty, S. Roy, S. Sen, *J. Cryst. Growth* 261 (2004) 77–81.
- [22] H. Saylikan, *Appl. Catal. A: Gen.* 319 (2007) 230–236.
- [23] K.R. Wu, C.W. Yeh, C.H. Hung, T.P. Cho, W.J. Liu, *J. Nanosci. Nanotechnol.* 9 (2009) 3433–3440.
- [24] F.R. Sensato, R. Custodio, A. Elson Longo, J. Beltrán, Andrés, *Catal. Today* 85 (2003) 145–152.
- [25] F. Fresno, D. Tudela, J.M. Coronado, M. Fernández-García, A.B. Hungría, J. Soria, *Phys. Chem. Chem. Phys.* 8 (2006) 2421–2430.
- [26] J. Yu, S. Liu, M. Zhou, *J. Phys. Chem. C* 112 (2008) 2050–2057.
- [27] F. Fresno, D. Tudela, J.M. Coronado, J. Soria, *Catal. Today* 143 (2009) 230–236.
- [28] R.K. Gupta, K. Ghosh, S.R. Mishra, P.K. Kahol, *Appl. Surf. Sci.* 253 (2007) 9422–9425.
- [29] O. Zywitzki, T. Modes, H. Sahm, P. Frach, K. Goedcke, D. Glöß, *Surf. Coat. Technol.* 180–181 (2004) 538–543.
- [30] M. Kitano, M. Takeuchi, M. Matsuoka, J.M. Thomas, M. Anpo, *Catal. Today* 120 (2007) 133–138.
- [31] K. Kalayanansundaram, M. Grätzel, *Coord. Chem. Rev.* 77 (1998) 347–414.
- [32] M. Radecka, *Thin Solid Films* 451–452 (2004) 98–104.
- [33] O. Zywitzki, T. Modes, P. Frach, D. Glöss, *Surf. Coat. Technol.* 202 (2008) 2488–2493.
- [34] C.H. Yi, I. Yasui, Y. Shigesato, *Jpn. J. Appl. Phys.* 34 (1995) 1638–1642.
- [35] R. Hengerer, L. Kavan, P. Krtík, M. Grätzel, *J. Electrochem. Soc.* 147 (2000) 1467–1472.
- [36] H.G. Yang, C.H. Sun, S.Z. Qiao, J. Zou, G. Liu, S.C. Smith, H.M. Cheng, G.Q. Lu, *Nature* 453 (2008) 638–641.
- [37] J. Yu, J. Xiong, B. Cheng, S. Liu, *Appl. Catal. B: Environ.* 60 (2005) 211–221.
- [38] A.S. Barnard, L.A. Curtiss, *Nano Lett.* 5 (2005) 1261–1266.
- [39] R.L. Penn, J.F. Banfield, *Geochim. Cosmochim. Acta* 63 (1999) 1549–1557.
- [40] J.C. Yu, X. Wang, X. Fu, *Chem. Mater.* 16 (2004) 1523–1530.
- [41] A. Mills, G. Hill, M. Crow, S. Hodgen, *J. Appl. Electrochem.* 35 (2005) 641–653.
- [42] Y. Zhao, X. Zhang, J. Zhai, J. He, L. Jiang, Z. Liu, S. Nishimoto, T. Murakami, A. Fujishima, D. Zhu, *Appl. Catal. B: Environ.* 83 (2008) 24–29.
- [43] H. Zhu, B. Yang, J. Xu, Z. Fu, M. Wen, T. Guo, S. Fu, J. Zuo, S. Zhang, *Appl. Catal. B: Environ.* 88 (2009) 525–532.
- [44] C. Tai, J.F. Peng, J.F. Liu, G.B. Jiang, H. Zoub, *Anal. Chim. Acta* 527 (2004) 73–80.
- [45] A. Brudnik, A. Gorzowska-Sobas, E. Pamuła, M. Radecka, K. Zakrzewska, *J. Power Sources* 173 (2007) 774–780.
- [46] M. Toyoda, Y. Nanbu, Y. Nakazawa, M. Hirano, M. Inagaki, *Appl. Catal. B: Environ.* 49 (2004) 227–232.
- [47] M. Inagaki, R. Nonaka, B. Tryba, W. Antoni, Morawski, *Chemosphere* 64 (2006) 437–445.
- [48] F. Fabregat-Santiago, J. Bisquert, E. Palomares, L. Otero, D. Kuang, S.M. Zakeeruddin, M. Grätzel, *J. Phys. Chem. C* 111 (2007) 6550–6560.
- [49] Y. Wang, H. Cheng, Y. Hao, J. Ma, W. Li, S. Cai, *Thin Solid Films* 349 (1999) 120–125.
- [50] L. Kavan, M. Grätzel, *Electrochim. Acta* 40 (1995) 643–652.
- [51] M. Radecka, P. Pasierb, K. Zakrzewska, M. Rekas, *Solid State Ionics* 119 (1999) 43–48.
- [52] M.J. Alam, D.C. Cameron, *Thin Solid Films* 420–421 (2002) 76–82.
- [53] T. Bak, J. Nowotny, M. Rekas, C.C. Sorrell, *Int. J. Hydrogen Energy* 27 (2002) 991–1022.
- [54] K.R. Reyes-Gil, E.A. Reyes-Garcia, D. Raftery, *J. Phys. Chem. C* 111 (2007) 14579–14588.